Inorganic Chemistry

pubs.acs.org/IC Article

Enhancing Stability of SAPO-37 Molecular Sieve through Aluminum Phosphate Utilization: Synthesis, Stability Mechanism, and Catalytic Performance

Runyu Ma,[‖] Yida Zhou,[‖] Huifang Wu, Jincong Wang, Xin Yan, Wei Huang, Tianlong Wang, Shutao Xu,* and Limin Ren*

Cite This: *Inorg. Chem.* 2024, 63, 14539−14549 Read Online

ACCESS | Metrics & More | Article Recommendations | Supporting Information

ABSTRACT: SAPO-37 molecular sieve, characterized by its three-dimensional 12-membered-ring FAU structure, has drawn wide attention due to its unique properties and catalytic potential. However, its susceptibility to framework collapse under low-temperature and humid conditions hinders practical applications, affecting both the reaction performance and sample storage. To tackle this, we utilized aluminum phosphate as a precursor for synthesizing SAPO-37, aiming to modify Si incorporation mechanisms and improve P and Al environments. Solid NMR spectroscopy combined with other techniques proves that the resulting SAPO-37-AP has enriched silicon islands, leading to reduced water adsorption, more reversible structural change, and significantly enhanced stability after low-temperature vapor treatment compared to conventional SAPO-37. Remarkably, SAPO-37-AP, after water vapor treatment, still exhibits superior performance in the liquid-phase Beckmann rearrangement reaction. This approach enhances stability, reduces templating agent amounts, and improves the solid product yield, offering promising practical applications.

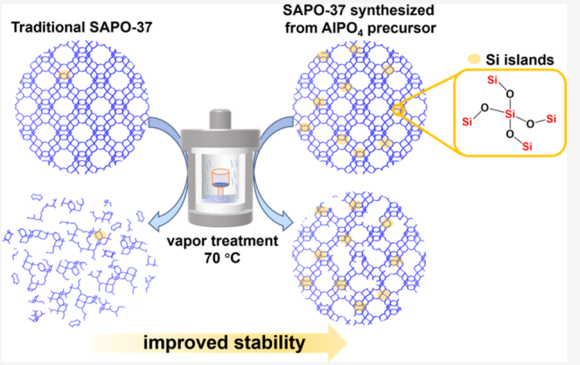

1. INTRODUCTION

The synthesis of aluminophosphate molecular sieves ($AlPO_4$-*n*) in the 1980s introduced a new branch in molecular sieves.[1] $AlPO_4$-*n* features a neutral framework of alternating AlO_4 and PO_4 tetrahedra.[2] In 1984, Flanigen et al. introduced silicon atoms into the framework, leading to the development of silicoaluminophosphate (SAPO-*n*) molecular sieves.[3] The negatively charged framework endows SAPO-*n* molecular sieves with Brønsted acid sites, offering milder acidity compared to aluminosilicate molecular sieves, thereby expanding the application of molecular sieves in the field of catalysis.[4−8]

SAPO-37 molecular sieve shares the FAU topology like the industrially widely used Y zeolite.[3] With a three-dimensional 12-membered ring pore structure (12-MR, formed by the ordered connection of SOD cages through the double 6-membered ring) and large supercages, this microporous material has attracted the attention of researchers since its discovery.[9−16] Unlike Y zeolite, the framework of SAPO-37 primarily consists of P and Al atoms, with Si partially substituting some P atoms through the SM2 mechanism.[17] This results in the majority of Si existing in the form of Si(4Al) in SAPO-37, leading to a significant number of Brønsted acid sites.[17,18] The acidity of SAPO-37 is notably milder compared to Y zeolite,[19] making it advantageous in weak acid catalysis applications.[14−16,20] For example, in the liquid-phase Beckmann rearrangement reaction of cyclohexanone oxime, SAPO-37 demonstrated superior activity and selectivity when compared to traditional ZSM-5 and Y zeolites.[16] The structural and acidity features also make SAPO-37 a useful candidate in plastic degradation,[21] olefin isomerization,[22] as well as being a support material.[9,10]

Unfortunately, in practical applications, SAPO-37 faces significant challenges, particularly when exposed to water vapor. After calcination to remove the template agents, SAPO-37 is prone to framework deformation and collapse under low-temperature conditions.[11,19,23] In 1987, Davis et al. first proposed that SAPO-37 was sensitive to humid environments.[18] Further investigation confirmed that its instability was mainly in the low-temperature region (T < 345 K), where SAPO-37 irreversibly lost its crystallinity under low-temperature and humid conditions,[24,25] despite its excellent stability in high-temperature environments (up to 1300 K).[24,26] The instability not only caused SAPO-37 to be sensitive to

Received: May 2, 2024
Revised: July 8, 2024
Accepted: July 11, 2024
Published: July 20, 2024

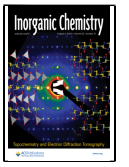

https://doi.org/10.1021/acs.inorgchem.4c01816
Inorg. Chem. 2024, 63, 14539−14549

reactions involving water but also resulted in a great challenge in sample storage. Usually, cautious storage (in an anhydrous atmosphere)[10,22] or partial retention of the SDA is required to stabilize the SAPO-37 framework,[13,27,28] causing high cost and limited utilization of active sites.

To enhance the stability of SAPO-37, understanding its instability mechanism is crucial. Davis et al. highlighted the hydrophilicity of SAPO-37 due to its high silica content, leading to the postcalcination of numerous −OH groups.[18] Barthormeuf et al. proposed that Si substitution mechanisms and unit cell parameters contribute to its low stability compared to SAPO-5.[24] Some explanations indicate that high-temperature calcination may lead to the formation of unfavorable P−O−P bonds, prone to hydrolysis,[29] or alter T−O−T bond angles,[30] ultimately causing framework collapse. Hunger et al. demonstrated that water molecules adsorb onto Brønsted acidic bridging OH groups (Si−OH−Al), resulting in framework breakdown.[31] Kalantzopoulos et al. emphasized that trapped water molecules between the SOD cage and the double 6-MR lead to the framework fracture at low temperatures.[11] Collectively, these studies indicate that the intrinsic properties, such as the status of Si, the hydrophilicity, and the overall T−O environment, are critical in affecting the stability of calcined SAPO-37 at low temperatures when exposed to humidity.

Considering these findings, modifying the Si, P, and Al environments within SAPO-37 could potentially enhance its stability. One effective approach is altering the precursors' form to influence the interaction manner of Si, P, and Al species, thereby impacting hydrolysis and growth behavior. In this study, aluminum phosphate was chosen as a precursor to synthesize a SAPO-37 molecular sieve, aiming to improve stability in low-temperature humid environments. Unlike traditional approaches using separate phosphoric acid and pseudoboehmite sources, which can readily form isolated ions from P or Al species, aluminum phosphate combines phosphorus and aluminum in a bonded form and is insoluble under ambient mild conditions. This unique feature could alter the hydrolysis and growth mode of P and Al atoms, thereby influencing the formation order and pattern of different bonds, including P−O−Al, Si−O−Al, and Si−O−Si bonds, crucial for SAPO molecular sieve stability.[31−33] Moreover, the already bonded aluminum phosphate may affect the Si substitution mechanism, potentially resulting in products with changed Si content and Si status.[34,35]

After optimization of the synthesis conditions, SAPO-37 (SAPO-37-AP) was successfully prepared using aluminum phosphate as the P and Al source. Remarkable stability enhancement and improved catalytic performance were observed after the low-temperature water vapor treatment. Solid-state NMR combined with other techniques were employed to elucidate the stability enhancement. Additionally, compared to traditional synthesis methods, this method significantly reduces the templating agent amount and enhances the solid product yield.

2. EXPERIMENTAL SECTION

2.1. Materials. The materials used for the synthesis of SAPO-37 molecular sieves were fumed silica (CAB-O-SIL M5), aluminum phosphate ($AlPO_4$, 95 wt %, Shanghai Titan Scientific Co., Ltd.), pseudoboehmite (Al_2O_3, 70 wt %, Dezhou Jinghuo Technology Glass Co., Ltd.), phosphoric acid (H_3PO_4, 85 wt %, Tianjin Damao Chemical Reagent Factory), tetrapropylammonium hydroxide (TPAOH, 40 wt %, Shanghai Annaiji Chemical Reagent Co.), and tetramethylammonium hydroxide pentahydrate ($TMAOH{\cdot}5H_2O$, 98 wt %, Shanghai Annaiji Chemical Reagent Co.). The materials used in the catalytic tests were cyclohexanone oxime (98 wt % Shanghai Annaiji Chemical Reagent Co.), benzonitrile (99 wt %, Shanghai Annaiji Chemical Reagent Co.), caprolactam (99 wt %, Shanghai Aladdin Biochemical Technology Co., Ltd.), and chlorobenzene (99.5 wt %, Tianjin Damao Chemical Reagent Factory).

2.2. Preparation of SAPO-37 Using Aluminum Phosphate (SAPO-37-AP). As a typical run, the preparation method of SAPO-37-AP was as follows. First, a certain amount of fumed silica, aluminum phosphate, tetramethylammonium hydroxide pentahydrate ($TMAOH{\cdot}5H_2O$), and tetrapropylammonium hydroxide (TPAOH, 40 wt %) were mixed. After grinding for 15−20 min, the composition of the initial gel was: 1.0 SiO_2:2.0 $AlPO_4$:0.05x TMAOH:2x TPAOH:9.3−34.9 H_2O, where x = 1.0, 0.75, 0.50, 0.44, 0.38, and 0.25. The homogeneous gel was transferred to a Teflon-lined stainless-steel autoclave for static hydrothermal crystallization at 200 °C for 13 h. Then, the crystallized sample was washed with deionized water and dried at 100 °C for 12 h, denoted as SAPO-37-AP. The obtained as-synthesized sample was calcined at 550 °C for 8 h.

2.3. Preparation of Conventional SAPO-37 (SAPO-37-C). Conventional SAPO-37, denoted as SAPO-37-C, was prepared according to a reported method,[36] the initial gel composition was: 1.0 SiO_2:1.0 Al_2O_3:1.0 P_2O_5:0.05 TMAOH:2.0 TPAOH:50 H_2O. First, in a solution containing 5.518 g of deionized water and 6.144 g of phosphoric acid, 3.882 g of pseudoboehmite was added and stirred for 8 h to prepare solution 1. Next, 0.24 g of $TMAOH{\cdot}5H_2O$ was dissolved in 27.114 g of TPAOH (40 wt %) solution, and 1.6 g of fumed silica was added and stirred for 1 h to prepare solution 2. Solution 2 was added slowly to solution 1 and stirred for 24 h in order to achieve a homogeneous gel. The gel was transferred into a PTFE-lined autoclave and statically crystallized at 200 °C for 13 h. After cooling down to room temperature, the crystallized sample was washed with deionized water and dried at 100 °C for 12 h and then calcined at 550 °C for 8 h.

2.4. Characterization. The crystalline structure was characterized by using a Rigaku SmartLab 9 kW X-ray diffractometer with Cu Kα radiation source (λ = 0.15406 nm) at 45 kV and 200 mA. The 2θ range from 5 to 40° was recorded with a scanning speed of 10° min^{-1}. The pH value was measured by using a Shanghai Thunder Magnetic PHS-3C acidity meter. The morphology and size of the samples were observed using a JSM-7610 Plus field emission scanning electron microscope (SEM) with an accelerating voltage of 5 kV. The textural properties of the samples were measured by a Micromeritics 3Flex instrument, and the samples were evacuated at 200 °C for 5 h. The specific surface area and micropore volume of the samples were calculated using the Brunauer−Emmett−Teller (BET) equation and the t-plot method, respectively. The pore size distribution was determined by the nonlocal density functional theory (NLDFT) method. Transmission electron microscopy (TEM) images were obtained using a Hitachi HT7700 EXALENS field-emission transmission electron microscope operated at 100 kV. The ultraviolet (UV) Raman spectra were recorded by a homemade UV Raman spectrometer with a spectral resolution of 2 cm^{-1}. A 244 nm laser line from an intracavity dual-frequency Lexel laser (Lexel Inc.) was used as the excitation source, and the laser power was about 3 mW. Thermogravimetric analysis was performed on a Netzsch STA449F3 synchronous thermal analyzer by heating in air from 30 to 800 °C at a ramp rate of 10 °C min^{-1}. Pyridine adsorption infrared (Py-IR) spectroscopy was carried out on a German Bruker Equinox 55 spectrometer with a resolution of 4 cm^{-1} using a homemade quartz vacuum cell with a KBr window. The sample was evacuated at 350 °C for 30 min, then exposed to pyridine at room temperature and adsorbed for 15 min. Desorption was performed under vacuum conditions at 150 °C. Temperature-programmed desorption of ammonia (NH_3-TPD) was measured by using a PCA-1200 chemical adsorption instrument. Then, 75 mg of sample was placed at the bottom of a quartz reactor and activated at 500 °C for 1 h under argon flow (30 mL min^{-1}) and adsorbed NH_3 for 40 min when

https://doi.org/10.1021/acs.inorgchem.4c01816
Inorg. Chem. 2024, 63, 14539−14549

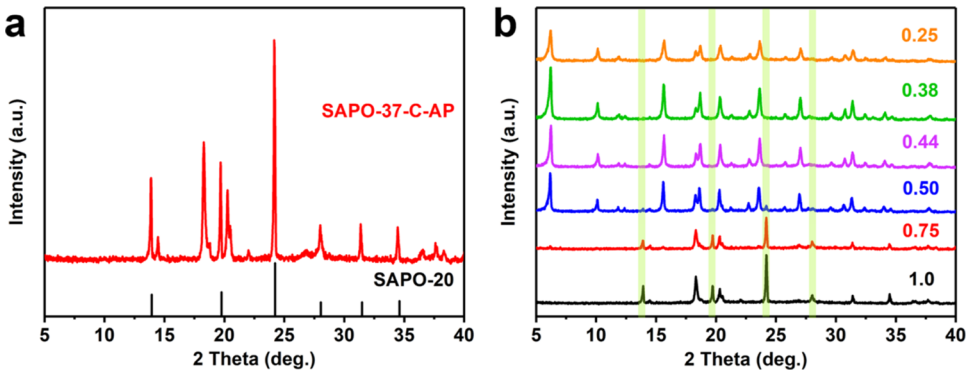

Figure 1. XRD patterns of (a) SAPO-37-C-AP synthesized by directly using aluminum phosphate as a precursor in the conventional synthesis system with chemical composition of 1.0 SiO_2:1.0 Al_2O_3:1.0 P_2O_5:0.05 TMAOH:2.0 TPAOH:50 H_2O and (b) SAPO-37-AP synthesized with different OSDAs/SiO_2 ratios (green region: SAPO-20), with the chemical composition of 1.0 SiO_2:2.0 $AlPO_4$:0.25−1.0 OSDAs (TPAOH/TMAOH = 40):9.3−34.9 H_2O.

cooled to 150 °C. Then, the sample was purged with argon at 150 °C for 40 min to remove the physically adsorbed NH_3. NH_3-TPD was carried out under a constant flow of argon from 120 to 650 °C at a rate of 10 °C min^{-1} and was detected by a thermal conductivity detector (TCD). The chemical composition of the samples was determined by a PerkinElmer Avio 220 ICP-OES. Ten milligrams of sample was taken, dissolved in hydrofluoric acid, and diluted to 25 mL with water. ^{27}Al, ^{29}Si, and ^{31}P experiments were performed on a Bruker Avance III 600 spectrometer equipped with a 14.1 T and 89 mm wide-bore magnet using a 4 mm HX double resonances MAS probe with the corresponding Larmor frequencies of 156.38, 119.23, and 242.94 MHz, respectively. The chemical shifts were referenced to 1 mol L^{-1} aluminum nitrate [$\delta(^{27}Al)$ = 0 ppm], kaolinite [$\delta(^{29}Si)$ = −91.5 ppm] and ammonium dihydrogen phosphate [$\delta(^{31}P)$ = 1.11 ppm]. ^{27}Al MAS NMR experiments were performed with a $\pi/12$ pulse width of 0.4 μs; 2560 scans were accumulated with a spinning rate of 10 kHz and a recycle delay of 0.2 s. ^{29}Si MAS NMR experiments were performed with a $\pi/4$ pulse width of 2.9 μs with ^1H decoupling; 4096 scans were accumulated with a spinning rate of 10 kHz and a recycle delay of 10 s. ^{31}P MAS NMR experiments were performed with a $\pi/4$ pulse width of 1.95 μs with ^1H decoupling; 16 scans were accumulated with a spinning rate of 10 kHz and a recycle delay of 20 s.

2.5. Stability Tests. *2.5.1. Low-Temperature Vapor Stability Test.* A 0.1 g portion of the freshly calcined sample was packed into a small Teflon cylinder cup (height: 2 cm; bottom diameter: 3 cm) and placed in a 100 mL PTFE-lined autoclave with 2 g of solvent (deionized water, methanol, or ethanol) at the bottom. The autoclave was sealed and heated in an oven at 70 °C for 5 h.

2.5.2. Medium and High-Temperature Water Vapor Stability Test. In the steam generator (HSG02, HuaXiangStar), 100% water vapor was pumped into a temperature-controlled tube furnace at a flow rate of 0.1 g min^{-1}, where the freshly calcined sample was located. The treatment was performed at 500 °C (medium temperature) or 850 °C (high temperature) for 12 h, separately.

2.6. Catalytic Tests. In a 50 mL round-bottom flask, 0.1 g of cyclohexanone oxime, 20 mL of benzonitrile, and a catalyst were added. Chlorobenzene was added as the internal standard. The flask was placed in a temperature-controlled oil bath at 140 °C for 6 h of reflux. After the reaction, the supernatant was taken and analyzed by gas chromatography (Agilent 8860, HP-5MS column, 30 m × 0.32 mm × 0.25 μm, FID detector). After the reaction, the catalyst was recycled. The solid catalyst was filtered and washed with ethanol three times, dried at 100 °C for 12 h, and followed by calcination at 550 °C in a box furnace for 8 h. Then, the reactions were tested using the recycled catalyst. The conversion, yield, and selectivity were calculated as

$$\text{conversion} = (\text{initial moles of oxime} - \text{moles of oxime detected}) / (\text{initial moles of oxime}) \times 100\%$$

$$\text{yield} = (\text{moles of caprolactam detected}) / (\text{initial moles of oxime}) \times 100\%$$

$$\text{selectivity} = (\text{moles of caprolactam detected}) / (\text{initial moles of oxime} - \text{moles of oxime detected}) \times 100\%$$

3. RESULTS AND DISCUSSION

3.1. Optimization of Synthesis Conditions Using Aluminum Phosphate to Obtain SAPO-37-AP. The synthesis of SAPO-37 using aluminum phosphate as the phosphorus and aluminum sources was first attempted by directly replacing pseudoboehmite and phosphoric acid without changing other synthetic parameters in the recipe for the conventional SAPO-37 synthesis.[36] However, the resulting product, SAPO-37-C-AP, primarily consisted of SAPO-20 and aluminum phosphate, failing to yield SAPO-37 as intended, as depicted in Figure 1a. Typically, conventional SAPO-37 (SAPO-37-C) is synthesized within a pH range of approximately 8 to 10, using both tetramethylammonium hydroxide (TMAOH) and tetrapropylammonium hydroxide (TPAOH) as organic structure directing agents (OSDAs).[36] Substituting phosphoric acid with aluminum phosphate led to an increase in the alkalinity of the synthesis system, potentially deviating from the optimal pH range (Table S1). To address this pH discrepancy, a reduction in the number of OSDAs was necessary. In the meantime, in order to improve the product yield, we also reduced the water content of the synthetic gel. By optimizing the OSDA content and adjusting the chemical composition, highly crystalline SAPO-37 was successfully obtained with the chemical composition of 1.0 SiO_2:2.0 $AlPO_4$:0.38−0.44 OSDAs (with TPAOH/TMAOH = 40):13.7−15.8 H_2O, as illustrated in Figure 1b. As the OSDAs/SiO_2 ratio decreases, the diffraction peaks of SAPO-20 and aluminum phosphate gradually weaken, with the SAPO-20 peak completely disappearing at a ratio of 0.44. Concurrently, diffraction peaks characteristic of SAPO-37 emerged, with peak intensity peaking at a ratio of 0.38, corresponding to a gel pH of 10.12 (Table S1). Further

https://doi.org/10.1021/acs.inorgchem.4c01816
Inorg. Chem. 2024, 63, 14539−14549

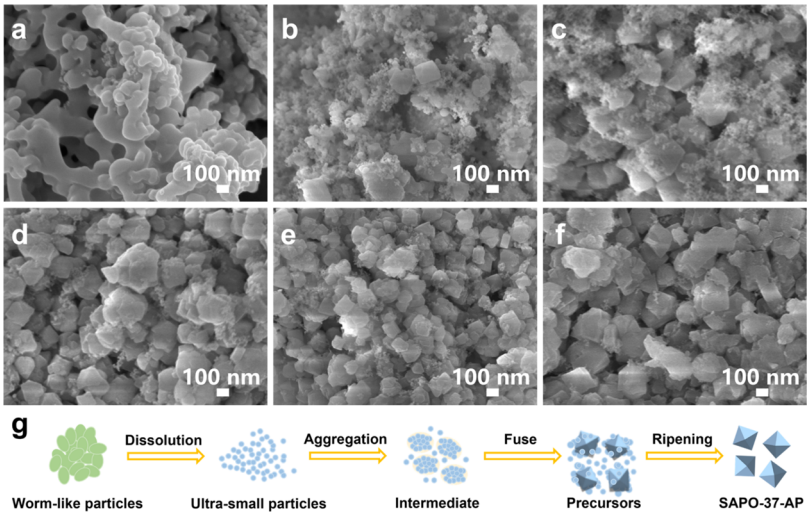

Figure 2. SEM images of SAPO-37-AP crystallized at 200 °C for (a) 0, (b) 3, (c) 5, (d) 7, (e) 10, and (f) 13 h. (g) Schematic representation of the growth process of SAPO-37-AP.

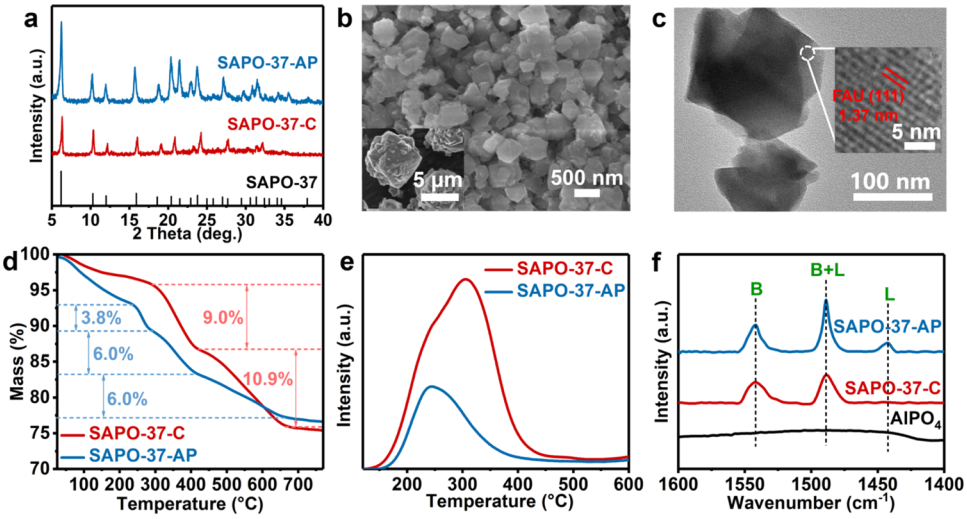

Figure 3. (a) XRD patterns of SAPO-37-AP and SAPO-37-C after calcination. (b) SEM image of SAPO-37-AP (inset: SEM image of SAPO-37-C), (c) TEM image of SAPO-37-AP (inset: HRTEM image), (d) TG curves, and (e) NH_3-TPD profiles of SAPO-37-AP and SAPO-37-C, (f) pyridine FTIR spectra of different samples.

reduction in the OSDAs/SiO_2 ratio led to decreased crystallinity, possibly due to an insufficient directing effect.

Optimization of the crystallization temperature was conducted within the range of 140−200 °C, and the results are shown in Figure S1a. Similar to the conventional synthesis of SAPO-37-C, high temperature favors the crystallization of SAPO-37-AP. At a fixed crystallization time of 13 h, increasing the temperature led to the heightened peak intensity of SAPO-37-AP, while the peaks associated with aluminum phosphate gradually weakened. Lower temperatures required longer crystallization times and were less conducive to the transformation of aluminum phosphate (Figure S1b,c).

The growth process of SAPO-37-AP was monitored at 200 °C over a range of 0−13 h. X-ray diffraction (XRD) patterns (Figure S2) revealed a gradual decrease in aluminum phosphates and an increase in SAPO-37 characteristic peaks since its first emergence at 3 h, indicating that SAPO-37 growth gradually consumes aluminum phosphates. Interestingly, this consumption of aluminum phosphates is directly observed by SEM and TEM imaging (Figures 2 and S3). Prior to the hydrothermal treatment (0 h, Figures 2a and S3a), SEM and TEM images captured a large number of irregular worm-like particles, which are assigned to the aluminum phosphate according to the XRD observation (Figure S2). After 1 h of crystallization (Figure S3b), upon exposure to organic structural directing agents, worm-like particles show signs of etching, displaying bubble-like holes on their surfaces. Concurrently, ultrafine particles with a size of around 20 nm emerge, likely resulting from the dissolution of these worm-like particles. As the time was prolonged, at 2 h (Figure S3c), the ultrafine nanoparticles became the dominant species. After 3 h (Figures 2b and S3d), cubic-like products were born with abundant 20 nm particles adhering to their surfaces, corroborating the XRD result showing weak SAPO-37 peaks together with aluminum phosphate (Figure S2). As the crystallization progressed, the observed ultrasmall particles decreased while more octahedral crystals accumulated (Figure 2c−f), ultimately forming well-defined nanoscale crystals at 13 h. It is speculated that the ultrafine nanoparticles serve as the active species for further crystallization. The fusion of these

https://doi.org/10.1021/acs.inorgchem.4c01816
Inorg. Chem. 2024, 63, 14539−14549

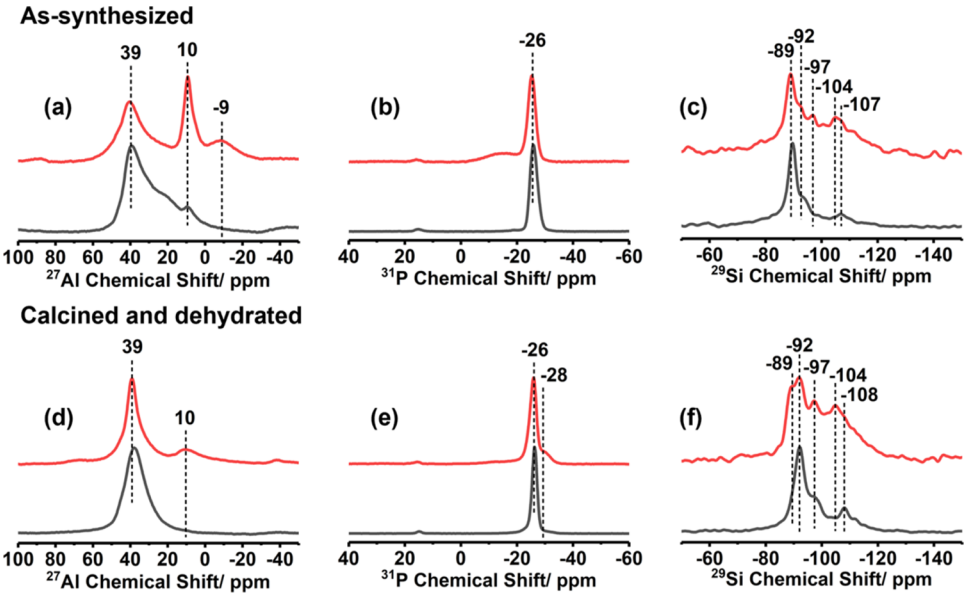

Figure 4. (a, d) ^{27}Al, (b, e) ^{31}P, and (c, f) ^{29}Si MAS NMR spectra of SAPO-37-C (black line) and SAPO-37-AP (red line) recorded in the as-synthesized and calcined forms. Before the measurement, the calcined form samples were dehydrated at 420 °C for 2 h to exclude the water adsorption effect.

nanoparticles facilitates the transition into SAPO-37 crystals. This dynamic evolution provides a plausible explanation for the formation of nanoscale crystals, whereby sustained growth of SAPO-37 occurs through the consumption of these small nanoparticles (Figure 2g).

3.2. SAPO-37-AP Characterization. The characterization of SAPO-37-AP synthesized at a crystallization temperature of 200 °C with SDA/SiO_2 = 0.38 is depicted in Figure 3. The XRD pattern of SAPO-37-AP after calcination (Figure 3a) reveals characteristic diffraction peaks of pure-phase FAU-type SAPO-37, and the peak intensity was higher than that of SAPO-37-C. The observed peak broadening of SAPO-37-AP could be attributed to its small particle size, as evidenced in the SEM image (Figure 3b). In comparison to SAPO-37-C, the crystal size of SAPO-37-AP notably decreased from the micrometer scale to the nanometer scale (Figure 3b). TEM imaging further confirms the small size of the SAPO-37-AP product, meanwhile revealing clear lattice fringes (Figure 3c), proving its good crystallinity. The interplanar distance of d = 1.37 nm corresponds to the (111) plane of the FAU crystal.

Moreover, due to the reduced water content in the synthesis gel, the calculated single-batch yield of SAPO-37-AP was 87.4%, significantly higher than that of the traditional synthesis method (23.4%). N_2 adsorption−desorption isotherms and pore size distribution results (Figure S4) indicate the presence of mesopores by the accumulation of small grains in SAPO-37-AP, with a specific surface area of 474 $m^2\ g^{-1}$, total pore volume of 0.38 $cm^3\ g^{-1}$, and micropore volume of 0.15 $cm^3\ g^{-1}$.

Thermogravimetric (TG) analysis (Figure 3d) revealed similar total mass loss for SAPO-37-AP and SAPO-37-C. However, the OSDA burning behaviors between the two samples are different (Figures 3d and S5). Apart from the mass loss caused by the removal of water (<200 °C), the SAPO-37-C sample exhibited two distinct stages of mass loss due to OSDA removal. Specifically, in the 280−400 °C range, the mass loss was linked to the removal of TPA^+ from the supercages, while the removal of TMA^+ from the sodalite cages occurred in the 400−700 °C range.[18] In contrast, SAPO-37-AP showed an additional stage of mass loss in the lower temperature range of 200−280 °C, likely due to the framework-bound water. Additionally, the mass loss in the 280−700 °C range suggested that SAPO-37-AP had fewer OSDAs trapped within its channels (12% mass loss) compared with SAPO-37-C (19.9% mass loss). This difference aligns with the smaller amount of OSDAs used in the preparation of SAPO-37-AP.

The acidic property of SAPO-37-AP is illustrated in Figure 3e,f. NH_3-TPD results (Figure 3e) indicated that SAPO-37-AP mainly consisted of weak acid and medium-strong acid (desorbed at 200−400 °C). The total acid site concentration was calculated to be 0.55 mmol g^{-1}, significantly lower than that of SAPO-37-C (1.32 mmol g^{-1}). With even slightly higher silicon content of SAPO-37-AP (Table S2, 0.18 of SAPO-37-AP vs 0.15 of SAPO-37-C, molar ratio), this acidity difference could be attributed to the Si distribution, which will be elaborated in the following ^{29}Si NMR characterization. Pyridine adsorption infrared (Py-IR) in Figure 3f clearly detected Brønsted acid sites (1541 cm^{-1}),[29] attributed to bridged hydroxyls (Si−OH−Al) formed by Si substitution in the framework replacing P. Furthermore, compared to SAPO-37-C, SAPO-37-AP also exhibited detectable Lewis acid sites (1442 cm^{-1}),[29] attributed to nonframework aluminum species. It is noteworthy that the calcined aluminum phosphate did not exhibit any acidity according to the Py-IR spectra, confirming that the residual aluminum phosphate was not the source of the Lewis acidity.

Further determination of the Si, P, and Al status and their local chemical environment was performed by solid-state MAS NMR spectroscopy. It is worth pointing out that before the NMR measurement, the calcined form sample was in situ dehydrated at 420 °C for 2 h to exclude the water adsorption effect. In the ^{27}Al MAS NMR spectra (Figure 4a), both as-synthesized samples show signals at 39 and 10 ppm, attributed respectively to tetracoordinated framework Al atoms (Al-$(OP)_4$) and pentacoordinated Al atoms.[31,37] Notably, an extra

https://doi.org/10.1021/acs.inorgchem.4c01816
Inorg. Chem. 2024, 63, 14539−14549

weak signal at −9 ppm appeared in SAPO-37-AP, indicating hexacoordinated Al atoms interacting with water molecules in the framework, in line with the TG result (Figure 3d).[31] Upon calcination (Figure 4d), the signal at 10 ppm in SAPO-37-AP weakened, while the signal at 39 ppm strengthened, suggesting a transformation of Al atoms from a pentacoordinated to a tetracoordinated state. The signal at −9 ppm disappeared, indicating the removal of bound water molecules due to the high-temperature calcination. Compared with SAPO-37-AP, the as-synthesized SAPO-37-C possesses a similar major tetracoordinated framework Al, with a much lower content of pentacoordinated Al. After calcination and further dehydration, only a peak centered at 39 ppm was observed, indicating the dominance of tetracoordinated framework Al states. The ^{27}Al NMR results are in good agreement with the pyridine IR result (Figure 3f) that SAPO-37-AP contained a small fraction of extraframework Al, resulting in Lewis acidity.

In the ^{31}P MAS NMR spectra (Figure 4b), both as-synthesized SAPO-37 samples show a sharp signal centered at −26 ppm, assigned to tetracoordinated framework P(OAl)$_4$ species,[37] while a weak and broad band at around −15 ppm was noticed in the SAPO-37-AP, which could be P atoms coordinated with water molecules.[31] After calcination and further dehydration (Figure 4e), with the removal of water, this broad band disappeared, accompanied by the appearance of a very weak signal at −28 ppm.[31] Based on ^{31}P NMR studies of early stage (0−2 h) SAPO-37-AP (Figure S6) samples, the signal at −28 ppm corresponds to tetrahedrally coordinated phosphorus atoms in residual aluminum phosphate. Interestingly, both the ^{31}P NMR and the ^{27}Al NMR suggest that the as-synthesized SAPO-37-AP is more like a hydrated form, in good agreement with the TG findings (Figure 3d). In addition, it is worth mentioning here that after calcination and dehydration, both samples possess quite sharp P signals, indicating the well-defined and uniform connection of the P−O−Al bonds associated with the highly crystalline structure. No P−O−P resonance peak was observed.

The ^{29}Si MAS NMR spectra revealed signals at −89 to −92 ppm assigned to tetracoordinated framework Si(OAl)$_4$ species (Figure 4c,4f).[15,37] Signals at −97, −104, and −108 ppm provided evidence of silicon clustering, corresponding respectively to Si(OAl)$_3$(OSi), Si(OAl)(OSi)$_3$, and Si(OSi)$_4$.[15] Although both SAPO-37 possess Si chemical shift peaks in similar positions, the distribution of the Si species are distinct, meaning the addition of aluminum phosphate altered the distribution of silicon. In line with the reported results, the predominant Si in the conventional SAPO-37 (SAPO-37-C) is in the isolated Si(4Al) form, as reflected in the main peak centered at around −90 ppm. In contrast, the SAPO-37-AP sample has more Si species with a higher chemical shift, which is evident in both the as-synthesized and the calcined samples and intensified after calcination. Especially the significantly higher portion of −108 ppm of Si(OSi)$_4$ species suggested more silicon islands in SAPO-37-AP, which was rarely reported in the traditional synthesis method. The significant difference in Si distribution could have resulted from a different Si substituting mechanism, which is closer to an SM2 + SM3 rather than the solely SM2 mechanism.[17] In the synthesis of SAPO-37-C, pseudoboehmite and phosphoric acid are used as dispersed sources of P and Al. During the reaction, these substances release more free Al and P ions. In this scenario, silicon readily forms connections with these free ions (Si−O−Al bonds) rather than self-assembling into Si−O−Si bonds. Therefore, fewer silicon islands are formed in SAPO-37-C. In contrast, in the synthesis of SAPO-37-AP, aluminum phosphate is used as the source of P and Al. The P and Al in aluminum phosphate exist in a stable, preconnected form as P−O−Al bonds. These bonds are relatively stable and are not easily broken during synthesis; thus, fewer free Al and P ions are released. This causes silicon atoms to preferentially self-assemble into Si−O−Si bonds. Consequently, SAPO-37-AP exhibits a higher presence of Si islands.

3.3. Stability Tests. The low-temperature stability test was performed at 70 °C using the setup as illustrated in Scheme 1.

Scheme 1. Low-Temperature Stability Test Setup

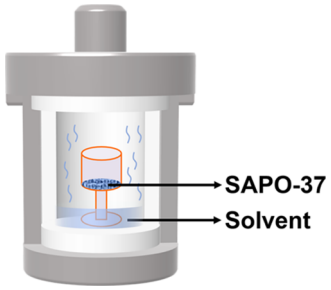

The stability of both SAPO-37-C and SAPO-37-AP was evaluated under vapors generated by water and different alcohols. Table 1 and Figure S7 summarize the effects of different solvent vapor treatment conditions on the crystallinity and micropore structure of SAPO-37-C and SAPO-37-AP, respectively. Under low-temperature alcohol vapor environments, SAPO-37-C maintains a good relative crystallinity, reaching up to 93.9% in ethanol. In addition, the N_2 sorption data indicate that there is no significant change in the micropore area, suggesting that alcohol vapor basically did not

Table 1. Relative Crystallinity and Relative Micropore Area of SAPO-37-C and SAPO-37-AP under Different Treatment Conditions

	SAPO-37-C		SAPO-37-AP	
conditions of treatment	relative crystallinity (%)[e]	relative micropore areas (%)[f]	relative crystallinity (%)[e]	relative micropore areas (%)[f]
untreated	100.0	100.0	100.0	100.0
water-850[a]	113.5	100.8	116.0	109.5
water-500[b]	94.6	99.8	107.7	101.8
water[c]	24.2	0	60.4	55.0
methanol[c]	84.4	92.7	105.1	99.2
ethanol[c]	93.9	96.6	96.4	94.4
water + alcohol[d]	83.0	64.2	92.6	80.1

[a]100% water vapor, flow rate of 0.1 g min^{-1}, 850 °C, 12 h. [b]100% water vapor, flow rate of 0.1 g min^{-1}, 500 °C, 12 h. [c]0.1 g sample, 2.0 g solvent, 70 °C, 5 h. [d]0.1 g sample, 2.0 g solvent (SAPO-37-C: ethanol, SAPO-37-AP: methanol, the mass ratio of water to alcohol was 1:9), 70 °C, 5 h. [e]Untreated samples were used as the reference samples, and their crystallinity was defined as 100%. Relative crystallinity = (sum of characteristic peak areas of other products)/(sum of characteristic peak areas of reference samples) × 100%. [f]Micropore areas (S_{micro}) were determined using the *t*-plot analysis. Untreated samples were used as the reference samples, and their micropore areas were defined as 100%. Relative micropore area = (micropore areas of other products)/(micropore areas of reference samples) × 100%.

https://doi.org/10.1021/acs.inorgchem.4c01816
Inorg. Chem. 2024, 63, 14539−14549

Scheme 2. Schematic Illustration of the Hydrolysis Process of the SAPO-37 Framework, (a) Water Adsorbed on Si−O−Al Sites, and Further Coordination with P−O−Al Bonds (b) without P−O−Al Bond Cleavage and (c) Causing P−O−Al Bond Cleavage

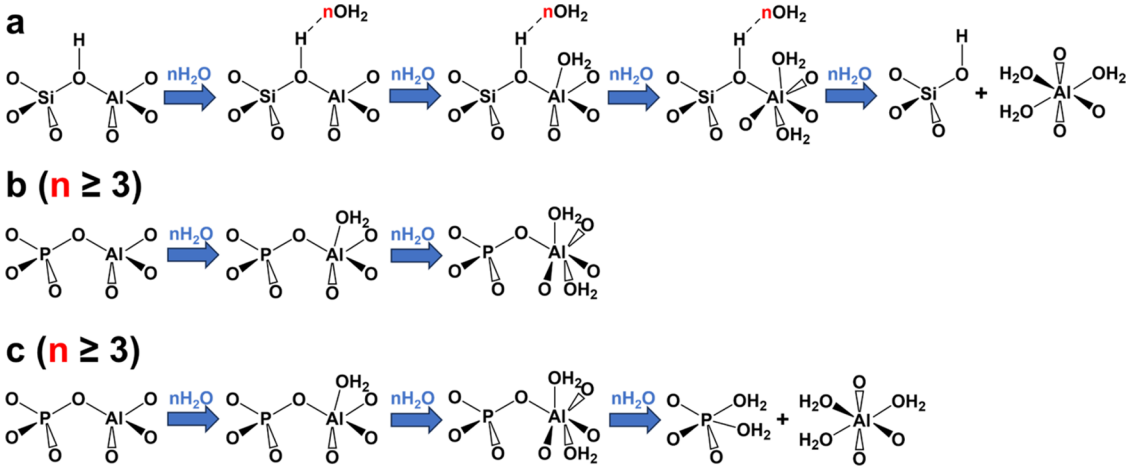

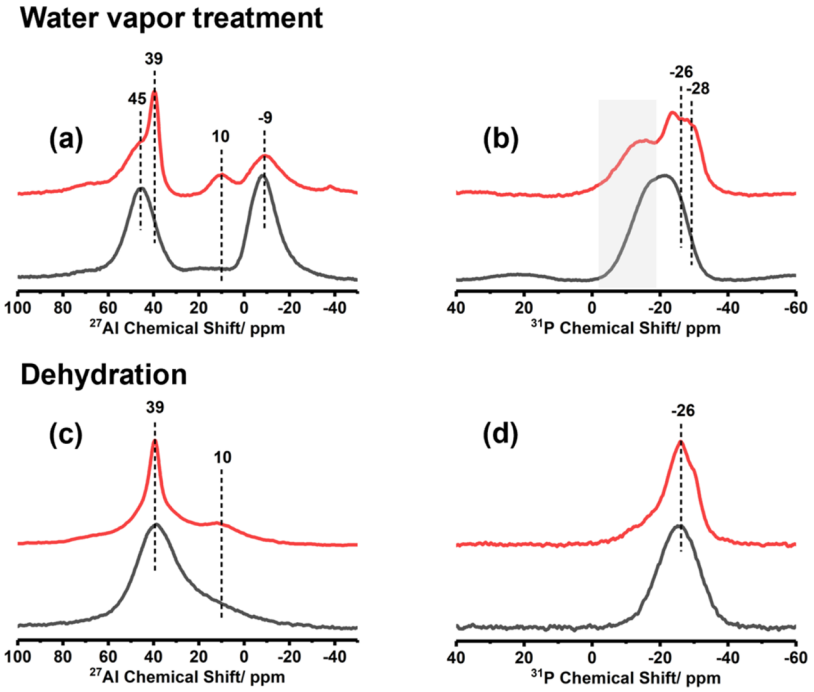

Figure 5. (a, c) ^{27}Al and (b, d) ^{31}P MAS NMR spectra of SAPO-37-C (black line) and SAPO-37-AP (red line) after water vapor treatment and further dehydration post vapor treatment.

disrupt the crystal structure, especially under ethanol vapor. However, when a small portion of water (10% of the total solvent mass) is mixed into ethanol, both the relative crystallinity and micropore area decrease substantially. This suggests that the framework of SAPO-37-C is susceptible to influence in the presence of water. Results from treatment under low-temperature water vapor further demonstrate the humidity sensitivity of SAPO-37-C. The relative crystallinity significantly decreases to 24.2% with the diminishing of the micropores, indicating a collapse of the framework structure. In great contrast, medium (500 °C) and high temperatures (850 °C) preserved or even strengthened the crystallinity of SAPO-37-C. The above results indicate that the SAPO-37-C framework with the templating agent removed is prone to collapse in low-temperature humid environments but exhibits excellent structural stability under medium- and high-temperature conditions, which is consistent with the reported results.[24,26]

When subjected to an alcohol vapor environment, SAPO-37-AP exhibited characteristics similar to those of SAPO-37-C, indicating minimal influence on the crystal structure by alcohols. Notably, under methanol vapor, the crystallinity of SAPO-37-AP was well preserved, contrasting with a 15% loss observed in SAPO-37-C. Additionally, the introduction of a small quantity of water in methanol (10% of the total solvent mass) had little effect on the structure, underscoring the low sensitivity of SAPO-37-AP to water. More importantly, under a low-temperature water vapor environment, the relative crystallinity of SAPO-37-AP is 60.4%, with a relative micropore area of 55.0%, indicating a much lesser degree of framework

https://doi.org/10.1021/acs.inorgchem.4c01816
Inorg. Chem. 2024, 63, 14539−14549

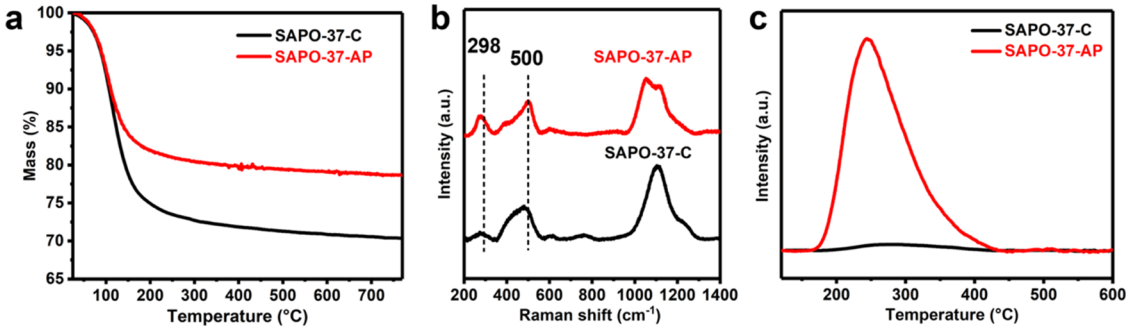

Figure 6. (a) TG curves, (b) UV Raman spectra, and (c) NH_3-TPD profiles of SAPO-37-AP and SAPO-37-C samples after water vapor treatment.

collapse compared to SAPO-37-C, thus demonstrating superior resistance to water-induced degradation. Meanwhile, SAPO-37-AP still retains the excellent stability characteristic of the SAPO-37 molecular sieve in medium- and high-temperature regions.

3.4. Stability Mechanism. The hydration process of silicoaluminophosphate molecular sieves consists of two parts.[31,38] Initially (Scheme 2a), water molecules adsorb onto the Brønsted acidic bridging hydroxyl groups (Si−OH−Al), causing the breaking of Si−O−Al bonds. After each bridging hydroxyl group adsorbs three or more water molecules, the water molecules also coordinate with aluminum atoms, resulting in two outcomes, namely, only simple coordination of water with the P−O−Al bonds (Scheme 2b) or cleavage of the P−O−Al bonds by hydrolysis (Scheme 2c). The breakage of Si−O−Al and P−O−Al bonds results in structural degradation.

A detailed comparison was conducted to examine the structural changes of the two samples after low-temperature water vapor treatment. Solid-state ^{31}P and ^{27}Al MAS NMR spectra are shown in Figure 5. After steam treatment, in the ^{27}Al MAS NMR spectra (Figure 5a), there was a shift in the signal of tetracoordinated Al (from 39 to 45 ppm), attributed to Brønsted acidic bridging hydroxyl groups (Si−OH−Al) adsorbing water molecules.[31,38] The main component of SAPO-37-C is $Si(OAl)_4$, which enhances its interaction with water, resulting in a stronger signal at 45 ppm, possibly causing the hydrolysis of the Si−O−Al bonds. SAPO-37-C exhibited a high-intensity signal at −9 ppm, whereas this signal in SAPO-37-AP was lower, indicating extensive hydrolysis or a significant amount of water within the structure of SAPO-37-C.[38,39] At the same time, additional signals appeared in the ^{31}P MAS NMR spectra between 0 and −20 ppm due to the coordination of P atoms with water molecules (Figure 5b), whereas those of SAPO-37-AP were notably lower than those of SAPO-37-C. It was again proven that SAPO-37-AP adsorbed less water.

Upon dehydration, the hexacoordinated Al atoms in water vapor-treated SAPO-37-AP reverted to tetracoordination, showing local structures nearly identical to those of the calcined sample (Figures 5c and S8a). However, SAPO-37-C exhibited a much broader peak centered at 39 ppm, representing Al in diverse forms and indicating irreversible effects (Figure S8c). In the ^{31}P MAS NMR spectra (Figure 5b), after exposure to water vapor, compared to SAPO-37-C, SAPO-37-AP exhibited weaker signals and a less broadening phenomenon between 0 and −20 ppm, associated with water-adsorbed P species. After dehydration (Figure 5d), both samples exhibited resonance peaks centered at −26 ppm, wider than the calcined samples (Figure S8b,d). Again, the peak broadening of SAPO-37-C is more prominent. This indicated that although low-temperature water vapor damaged the P−O−Al bonds in both samples, some of the fractured P−O−Al bonds in SAPO-37-AP would have reassembled. The extent of damage was more severe in SAPO-37-C, consistent with the results from XRD and N_2 adsorption−desorption (Table 1).

Collectively (Figure S8), following water vapor treatment, the Al signals of SAPO-37-AP showed a nearly reversible change upon further dehydration, contrasting the significant signal broadening of SAPO-37-C. In dehydrated SAPO-37-AP, the Al−OH formed by bond cleavage can coordinate with the surrounding Si atoms to form partially coordinated framework Al,[40] while some pentacoordinated Al atoms are also generated (10 ppm, Figure S8a). The P signals of both samples showed broadening after exposure to water vapor and dehydration, suggesting a certain degree of P−O−Al bond fracture, with SAPO-37-AP at a much lower level. Thereby, SAPO-37-AP is more resistant to the water vapor attack. It can be explained that in SAPO-37-AP, more Si existed in the silicon island form, with remaining less isolated and fragile Brønsted acidic bridging hydroxyl groups interacting with water molecules, thus leading to fewer fractured Si−O−Al bonds. Furthermore, the less adsorbed water molecules were beneficial in reducing the coordination of water with P−O−Al bonds within SAPO-37-AP, thereby reducing the level of irreversible bond cleavage. This phenomenon correlates with the observed variation in occluded water content post vapor treatment. The thermogravimetric curves in Figure 6a indicate a lower weight loss of the calcined SAPO-37-AP (21.3%) compared to SAPO-37-C (29.7%) after water vapor treatment, suggesting reduced water attack on the framework, thus contributing to its higher stability. However, in SAPO-37-C, almost all Brønsted acidic bridging hydroxyl groups coordinate with water molecules, resulting in severe P−O−Al bond damage, which is irreversible (Figure S8c,d). Additionally, after dehydration, a partial of the fractured P−O−Al bonds in SAPO-37-AP will be reassembled (Figure S8b), giving SAPO-37-AP excellent low-temperature stability.

UV Raman spectroscopy results from Figure 6b revealed that SAPO-37-AP contains a higher concentration of D6R (298 cm^{-1}) compared to SAPO-37-C after water vapor treatment. D6R and SOD cages were proposed to be the most sensitive building units to the humidity according to a recent study by Kalantzopoulos et al., where the water molecules tend to accumulate, thus causing framework degradation.[11] After water vapor treatment, a higher content of D6R was present in SAPO-37-AP, as observed from the relatively stronger and narrower 298 cm^{-1} Raman band,

https://doi.org/10.1021/acs.inorgchem.4c01816
Inorg. Chem. 2024, 63, 14539−14549

compared to SAPO-37-C, indicative of higher D6R retention and enhanced stability of SAPO-37-AP. NH_3-TPD results indicated that while SAPO-37-C experiences a near-total loss of acidity due to framework collapse, SAPO-37-AP experienced only partial loss of acid site number (0.35 mmol g^{-1} remaining), owing to its better stability (Figure 6c). Interestingly, after water vapor erosion, there was no significant change in the crystal morphology of the two samples (Figure S9).

3.5. Catalytic Performance Tests. Table 2 shows the catalytic performance of both catalysts in the liquid-phase Beckman rearrangement reaction before and after solvent vapor treatment. Different alcohols, selected based on minimal impact on the structural integrity of the samples, were employed for treatment. The results indicated that treatment by these alcohols had no significant effect on the catalytic activity of the SAPO-37 samples, attributed to negligible structural changes. Due to their excellent stability in medium and high-temperature water vapor environments, both SAPO-37 samples maintained good catalytic performance after treatment. After treatment with water vapor at 70 °C, the conversion of cyclohexanone oxime in the SAPO-37-C sample dramatically decreased to only 14.1% due to the nearly complete collapse of the structure and loss of acidity. In contrast, SAPO-37-AP retained an 86.0% conversion, attributed to the largely preserved structure and acidity (Figure 6c). Considering that a small amount of aluminum phosphate may remain in the calcined SAPO-37-AP sample, we also evaluated the conversion of cyclohexanone oxime by the aluminum phosphate postcalcination, which was only 0.08%, underscoring its minimal impact on the catalytic performance of SAPO-37-AP.

Table 2. Catalytic Performance of SAPO-37 Catalysts in the Liquid-Phase Beckmann Rearrangement Reaction

conditions of treatment	sample	results of catalysis[a] conversion (%)	yield (%)	selectivity (%)
untreated	SAPO-37-C	98.9	81.1	81.4
	SAPO-37-AP	93.3	75.8	81.2
alcohol vapor[b]	SAPO-37-C	98.5	82.7	84.0
	SAPO-37-AP	89.3	77.9	87.2
water vapor-850[c]	SAPO-37-C	99.0	81.6	82.4
	SAPO-37-AP	94.7	76.1	80.4
water vapor-500[d]	SAPO-37-C	92.8	79.4	85.6
	SAPO-37-AP	91.5	73.8	80.7
water vapor[e]	SAPO-37-C	14.1	12.7	90.1
	SAPO-37-AP	86.0	72.5	84.3
add water[f]	SAPO-37-C	43.2	36.9	85.4
	SAPO-37-AP	95.3	76.6	80.3

[a]Reaction conditions: 0.1 g cyclohexanone oxime, 0.1 g SAPO-37-C or 0.2 g SAPO-37-AP based on acid concentration, 20 mL benzonitrile, 140 °C, 6 h. [b]Conditions of treatment: 0.1 g sample, 2.0 g solvent (SAPO-37-C: ethanol, SAPO-37-AP: methanol), 70 °C, 5 h. [c]Conditions of treatment: 100% water vapor, flow rate of 0.1 g min^{-1}, 850 °C, 12 h. [d]Conditions of treatment: 100% water vapor, flow rate of 0.1 g min^{-1}, 500 °C, 12 h. [e]Conditions of treatment: 0.1 g sample, 2.0 g water, 70 °C, 5 h. [f]Conditions of treatment: 0.1 g deionized water was added directly to the reaction mixture before heating.

Furthermore, an experiment involving the direct addition of 0.1 g of water (0.5% of the solvent volume) into the reaction system provided a more straightforward demonstration of the stability of SAPO-37-AP. It has been reported that the direct addition of a small amount of water to the reaction mixture can alleviate the hydrolysis of cyclohexanone oxime to form cyclohexanone,[41] attributing to the chemical adsorption of water on Lewis acid sites, hindering side reactions.[41] SAPO-37-C retained less than half of its original conversion, while SAPO-37-AP maintained excellent catalytic activity, even showing a slight increase compared with the water-free reaction system. The lower sensitivity to water vapor and the presence of Lewis acidity in SAPO-37-AP both contribute to this activity enhancement. This observation intuitively demonstrates the outstanding stability of SAPO-37-AP. Additionally, as shown in Figure 7, recycling tests were performed on the water-treated SAPO-37-AP sample, demonstrating that the sample maintained good catalytic activity after five consecutive catalytic tests.

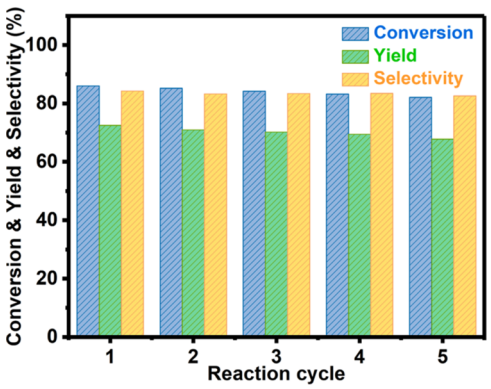

Figure 7. Recycling test of the SAPO-37-AP catalyst after water vapor treatment for caprolactam production. Reaction conditions: 0.2 g catalyst, 0.1 g cyclohexanone oxime, 20 mL benzonitrile, 140 °C, 6 h.

4. CONCLUSIONS

In conclusion, the study focused on enhancing the stability of SAPO-37 molecular sieves in low-temperature humid environments by using aluminum phosphate as a precursor during synthesis. Through optimized synthesis conditions, SAPO-37-AP was successfully prepared, showcasing notable stability improvements. Solid-state NMR and other techniques provided insights into the stability mechanisms of SAPO-37-AP, highlighting the role of aluminum phosphate in altering Si substitution mechanisms and minimizing irreversible bond breakage in the framework. The superior stability of SAPO-37-AP after water vapor treatment was evident in the liquid-phase Beckmann rearrangement reaction, with higher conversion rates attributed to retained crystallinity and total acidity. Reduced templating agent amount and increased solid yield further underscored the method's efficiency. These findings pave the way for the development of more stable and efficient SAPO-37 catalysts for diverse catalytic applications. It also offers a promising strategy for enhancing the stability of SAPO molecular sieves in challenging environmental conditions.

■ ASSOCIATED CONTENT

Supporting Information

The Supporting Information is available free of charge at https://pubs.acs.org/doi/10.1021/acs.inorgchem.4c01816.

https://doi.org/10.1021/acs.inorgchem.4c01816
Inorg. Chem. 2024, 63, 14539−14549

pH value of the initial gels by different preparation methods; other characterization of SAPO-37-C and SAPO-37-AP, including XRD patterns; N_2 adsorption−desorption isotherms; TG-derivative thermogravimetry (TG-DTG) curves; chemical compositions; solid-state NMR spectra, TEM and SEM images (PDF)

AUTHOR INFORMATION

Corresponding Authors

Shutao Xu − *National Engineering Research Center of Lower-Carbon Catalysis Technology, Dalian Institute of Chemical Physics, Chinese Academy of Sciences, Dalian 116023, P. R. China; State Key Laboratory of Catalysis, Dalian Institute of Chemical Physics, Chinese Academy of Sciences, Dalian 116023, P. R. China;* orcid.org/0000-0003-4722-8371; Email: xushutao@dicp.ac.cn

Limin Ren − *State Key Laboratory of Fine Chemicals, School of Chemistry, Dalian University of Technology, Dalian 116024, P. R. China;* orcid.org/0000-0002-9215-8280; Email: lren@dlut.edu.cn

Authors

Runyu Ma − *State Key Laboratory of Fine Chemicals, School of Chemistry, Dalian University of Technology, Dalian 116024, P. R. China*

Yida Zhou − *National Engineering Research Center of Lower-Carbon Catalysis Technology, Dalian Institute of Chemical Physics, Chinese Academy of Sciences, Dalian 116023, P. R. China; State Key Laboratory of Catalysis, Dalian Institute of Chemical Physics, Chinese Academy of Sciences, Dalian 116023, P. R. China*

Huifang Wu − *State Key Laboratory of Fine Chemicals, School of Chemistry, Dalian University of Technology, Dalian 116024, P. R. China*

Jincong Wang − *State Key Laboratory of Fine Chemicals, School of Chemistry, Dalian University of Technology, Dalian 116024, P. R. China*

Xin Yan − *State Key Laboratory of Fine Chemicals, School of Chemistry, Dalian University of Technology, Dalian 116024, P. R. China*

Wei Huang − *State Key Laboratory of Fine Chemicals, School of Chemistry, Dalian University of Technology, Dalian 116024, P. R. China*

Tianlong Wang − *State Key Laboratory of Fine Chemicals, School of Chemistry, Dalian University of Technology, Dalian 116024, P. R. China*

Complete contact information is available at: https://pubs.acs.org/10.1021/acs.inorgchem.4c01816

Author Contributions

[‖]R.M. and Y.Z. contributed equally to this work. This manuscript was written through contributions of all authors. All authors have given approval to the final version of the manuscript. R.M. performed catalyst preparation, characterization, stability and catalytic tests, and prepared the manuscript. Y.Z. participated in solid-state MAS NMR test, data analysis, and draft revision. H.W. performed SEM imaging and data analysis. J.W. performed TG test and reproduced the synthesis. X.Y. and W.H. performed TEM imaging and data analysis. T.W. performed the Py-IR test. S.X. participated in data analysis and draft revision. L.R. designed the study, analyzed the data, and revised the draft.

Notes

The authors declare no competing financial interest.

ACKNOWLEDGMENTS

The authors are grateful to the financial support of the National Natural Science Foundation of China (22372020; 22241801; 22022202; 21991092; 21991091; 21991090), Dalian Outstanding Young Scientist Foundation (2021RJ01), and the fund of the State Key Laboratory of Catalysis in DICP (N-21-02). The Large Instrument and Equipment Open Foundation of Dalian University of Technology and the Instrument Analysis Center of Dalian University of Technology are acknowledged too.

REFERENCES

(1) Wilson, S. T.; Lok, B. M.; Messina, C. A.; Cannan, T. R.; Flanigen, E. M. Aluminophosphate molecular sieves: a new class of microporous crystalline inorganic solids. *J. Am. Chem. Soc.* **1982**, *104* (4), 1146−1147.

(2) Li, S. S.; Chen, J.; Wang, Y.; Li, K. B.; Li, K. J.; Guo, W. J.; Zhang, X. R.; Liu, J. Q.; Tang, X.; Yang, J. F.; Li, J. P. Adsorption and separation of CH_4/N_2 by electrically neutral skeleton AlPO molecular sieves. *Sep. Purif. Technol.* **2022**, *286*, No. 120497.

(3) Lok, B. M.; Messina, C. A.; Patton, R. L.; Gajek, R. T.; Cannan, T. R.; Flanigen, E. M. Silicoaluminophosphate molecular sieves: another new class of microporous crystalline inorganic solids. *J. Am. Chem. Soc.* **1984**, *106* (20), 6092−6093.

(4) Wang, X. H.; Yan, N. N.; Xie, M.; Liu, P. X.; Bai, P.; Su, H. P.; Wang, B. Y.; Wang, Y. Z.; Li, L. B.; Cheng, T.; Guo, P.; Yan, W. F.; Yu, J. H. The inorganic cation-tailored "trapdoor" effect of silicoaluminophosphate zeolite for highly selective CO_2 separation. *Chem. Sci.* **2021**, *12* (25), 8803−8810.

(5) Li, Z. B.; Martínez-Triguero, J.; Concepción, P.; Yu, J. H.; Corma, A. Methanol to olefins: activity and stability of nanosized SAPO-34 molecular sieves and control of selectivity by silicon distribution. *Phys. Chem. Chem. Phys.* **2013**, *15* (35), 14670−14680.

(6) Beale, A. M.; Gao, F.; Lezcano-Gonzalez, I.; Peden, C. H. F.; Szanyi, J. Recent advances in automotive catalysis for NO_x emission control by small-pore microporous materials. *Chem. Soc. Rev.* **2015**, *44* (20), 7371−7405.

(7) Blasco, T.; Chica, A.; Corma, A.; Murphy, W. J.; Agúndez-Rodríguez, J.; Pérez-Pariente, J. Changing the Si distribution in SAPO-11 by synthesis with surfactants improves the hydroisomerization/dewaxing properties. *J. Catal.* **2006**, *242* (1), 153−161.

(8) Jin, D. L.; Ye, G. H.; Zheng, J. W.; Yang, W. M.; Zhu, K. K.; Coppens, M. O.; Zhou, X. G. Hierarchical silicoaluminophosphate catalysts with enhanced hydroisomerization selectivity by directing the orientated assembly of premanufactured building blocks. *ACS Catal.* **2017**, *7* (9), 5887−5902.

(9) Perez-Aguilar, J. E.; Hughes, J. T.; Chen, C. Y.; Gates, B. C. Transformation of atomically dispersed platinum in SAPO-37 into platinum clusters: catalyst for ethylene hydrogenation. *Catal. Sci. Technol.* **2021**, *11* (20), 6666−6681.

(10) Perez-Aguilar, J. E.; Chen, C. Y.; Hughes, J. T.; Fang, C. Y.; Gates, B. C. Isostructural atomically dispersed rhodium catalysts supported on SAPO-37 and on HY zeolite. *J. Am. Chem. Soc.* **2020**, *142* (26), 11474−11485.

(11) Kalantzopoulos, G. N.; Lundvall, F.; Thorshaug, K.; Lind, A.; Vajeeston, P.; Dovgaliuk, I.; Arstad, B.; Wragg, D. S.; Fjellvåg, H. Factors determining microporous material stability in water: the curious case of SAPO-37. *Chem. Mater.* **2020**, *32* (4), 1495−1505.

(12) Li, Y. X.; Wang, X.; Thersleff, T.; Svensson, G.; Hedin, N. Silicoaluminophosphate (SAPO)-Templated activated carbons. *ACS Omega* **2019**, *4* (6), 9889−9895.

(13) Thi, T. H. D.; Bartoszek, M.; Schneider, M.; Hoang, D. L.; Bentrup, U.; Martin, A. Chloride-free Cu-modified SAPO-37 catalyst

for the oxidative carbonylation of methanol in the gas phase. *Appl. Catal., B* **2012**, *121*, 115−122.
(14) Chapman, S.; Carravetta, M.; Miletto, I.; Doherty, C. M.; Dixon, H.; Taylor, J. D.; Gianotti, E.; Yu, J. H.; Raja, R. Probing the design rationale of a high-performing faujasitic zeotype engineered to have hierarchical porosity and moderated acidity. *Angew. Chem., Int. Ed.* **2020**, *59* (44), 19561−19569.
(15) Potter, M. E.; Chapman, S.; O'Malley, A. J.; Levy, A.; Carravetta, M.; Mezza, T. M.; Parker, S. F.; Raja, R. Understanding the role of designed solid acid sites in the low-temperature production of ε-caprolactam. *ChemCatChem* **2017**, *9* (11), 1897−1900.
(16) Potter, M. E.; O'Malley, A. J.; Chapman, S.; Kezina, J.; Newland, S. H.; Silverwood, I. P.; Mukhopadhyay, S.; Carravetta, M.; Mezza, T. M.; Parker, S. F.; Catlow, C. R. A.; Raja, R. Understanding the role of molecular diffusion and catalytic selectivity in liquid-phase Beckmann rearrangement. *ACS Catal.* **2017**, *7* (4), 2926−2934.
(17) Fyfe, C. A.; Wongmoon, K. C.; Huang, Y.; Grondey, H. Structural investigations of SAPO-37 molecular sieve by coherence-transfer and dipolar-dephasing solid-state nuclear magnetic resonance experiments. *Microporous Mater.* **1995**, *5* (1−2), 29−37.
(18) de Saldarriaga, L. S.; Saldarriaga, C.; Davis, M. E. Investigations into the nature of a silicoaluminophosphate with the faujasite structure. *J. Am. Chem. Soc.* **1987**, *109* (9), 2686−2691.
(19) Corma, A.; Fornes, V.; Franco, M. J.; Mocholi, F. A.; Perezpariente, J.Hydrothermal Stability and Cracking Behavior of Silicoaluminophosphate Molecular Sieve-37 with Different Silicon Contents. *ACS Symposium Series*; ACS Publications, 1991; *452*, 79−95.
(20) Potter, M. E.; Kezina, J.; Bounds, R.; Carravetta, M.; Mezza, T. M.; Raja, R. Investigating the role of framework topology and accessible active sites in silicoaluminophosphates for modulating acid-catalysis. *Catal. Sci. Technol.* **2018**, *8* (20), 5155−5164.
(21) Fernandes, G. J. T.; Fernandes, V. J.; Araujo, A. S. Catalytic degradation of polyethylene over SAPO-37 molecular sieve. *Catal. Today* **2002**, *75* (1−4), 233−238.
(22) Mostad, H. B.; Stocker, M.; Karlsson, A.; Rorvik, T. Comparison of the iso-structural H-SAPO-37 and H-faujasite as catalysts for the isobutane/2-butene alkylation. *Appl. Catal., A* **1996**, *144* (1−2), 305−317.
(23) Corma, A.; Fornes, V.; Perezpariente, J. SAPO-37: The implications of structure flexibility on acidity. *J. Chem. Soc., Chem. Commun.* **1993**, No. 8, 676−678.
(24) Briend, M.; Shikholeslami, A.; Peltre, M. J.; Delafosse, D.; Barthomeuf, D. Thermal and hydrothermal stability of SAPO-5 and SAPO-37 molecular sieves. *J. Chem. Soc., Dalton Trans.* **1989**, No. 7, 1361−1362.
(25) Simonot-Grange, M. H.; Waldeck, A.; Barthomeuf, D.; Weber, G. Contribution to the study of framework modification of SAPO-34 and SAPO-37 upon water adsorption by thermogravimetry. *Thermochim. Acta* **1999**, *329* (1), 77−82.
(26) Peltre, M. J.; Briend, M.; Lamy, A.; Barthomeuf, D.; Tauelle, F. Interaction of SAPO-37 molecular sieves with basic molecules: enhancement of stability. *J. Chem. Soc., Faraday Trans.* **1990**, *86* (22), 3823−3826.
(27) Spinacé, E. V.; Schuchardt, U.; Cardoso, D. Oxidation of hydrocarbons with peroxides catalyzed by chromium(III) and iron(III) incorporated in SAPO-37 framework. *Appl. Catal., A* **1999**, *185* (2), L193−L197.
(28) Malla, P. B.; Komarneni, S. Effect of pore size on the chemical removal of organic template molecules from synthetic molecular sieves. *Zeolites* **1995**, *15* (4), 324−332.
(29) Ojo, A. F.; Dwyer, J.; Dewing, J.; Karim, K. Synthesis and properties of SAPO-37. *J. Chem. Soc., Faraday Trans.* **1991**, *87* (16), 2679−2684.
(30) Kalantzopoulos, G. N.; Lundvall, F.; Lind, A.; Arstad, B.; Chernyshov, D.; Fjellvåg, H.; Wragg, D. S. SAPO-37 microporous catalysts: revealing the structural transformations during template removal. *Catal., Struct. React.* **2017**, *3* (1−2), 79−88.
(31) Buchholz, A.; Wang, W.; Arnold, A.; Xu, M.; Hunger, M. Successive steps of hydration and dehydration of silicoaluminophosphates H-SAPO-34 and H-SAPO-37 investigated by in situ CF MAS NMR spectroscopy. *Microporous Mesoporous Mater.* **2003**, *57* (2), 157−168.
(32) Parlitz, B.; Lohse, U.; Schreier, E. Hydrolysis of -P-O-Al- bonds in $AlPO_4$ and SAPO molecular sieves. *Microporous Mater.* **1994**, *2* (3), 223−228.
(33) Lourenço, J. P.; Ribeiro, M. F.; Ribeiro, F. R.; Rocha, J.; Gabelica, Z. Solid-state NMR and powder XRD studies of the structure of SAPO-40 upon hydration-dehydration cycles. *J. Chem. Soc., Faraday Trans.* **1995**, *91* (14), 2213−2215.
(34) Lin, C. L.; Cao, Y.; Feng, X.; Lin, Q. J.; Xu, H. D.; Chen, Y. Q. Effect of Si islands on low-temperature hydrothermal stability of Cu/SAPO-34 catalyst for NH_3-SCR. *J. Taiwan Inst. Chem. Eng.* **2017**, *81*, 288−294.
(35) Cao, Y.; Fan, D.; Zhu, D. L.; Sun, L. J.; Cao, L.; Tian, P.; Liu, Z. M. The effect of Si environments on NH_3 selective catalytic reduction performance and moisture stability of Cu-SAPO-34 catalysts. *J. Catal.* **2020**, *391*, 404−413.
(36) Franco, M. J.; Perezpariente, J.; Mifsud, A.; Blasco, T.; Sanz, J. Crystallization kinetics of SAPO-37. *Zeolites* **1992**, *12* (4), 386−394.
(37) Zhou, Y. D.; Shi, H. Z.; Wang, B. L.; Chen, G. R.; Yi, J.; Li, J. Y. The synthesis of SAPO-34 zeolite for an improved MTO performance: tuning the particle size and an insight into the formation mechanism. *Inorg. Chem. Front.* **2021**, *8* (9), 2315−2322.
(38) Yang, L.; Wang, C.; Zhang, L. N.; Dai, W. L.; Chu, Y. Y.; Xu, J.; Wu, G. J.; Gao, M. B.; Liu, W. J.; Xu, Z. C.; Wang, P. F.; Guan, N. J.; Dyballa, M.; Ye, M.; Deng, F.; Fan, W. B.; Li, L. D. Stabilizing the framework of SAPO-34 zeolite toward long-term methanol-to-olefins conversion. *Nat. Commun.* **2021**, *12* (1), No. 4661.
(39) Khoo, D. Y.; Kok, W. M.; Mukti, R. R.; Mintova, S.; Ng, E. P. Ionothermal approach for synthesizing AlPO-5 with hexagonal thin-plate morphology influenced by various parameters at ambient pressure. *Solid State Sci.* **2013**, *25*, 63−69.
(40) Chen, K.; Gan, Z.; Horstmeier, S.; White, J. L. Distribution of aluminum species in zeolite catalysts: ^{27}Al NMR of framework, partially-coordinated framework, and non-framework moieties. *J. Am. Chem. Soc.* **2021**, *143* (17), 6669−6680.
(41) Ngamcharussrivichai, C.; Wu, P.; Tatsumi, T. Catalytically active and selective centers for production of ε-caprolactam through liquid phase Beckmann rearrangement over H-USY catalyst. *Appl. Catal., A* **2005**, *288* (1−2), 158−168.

https://doi.org/10.1021/acs.inorgchem.4c01816
Inorg. Chem. 2024, 63, 14539−14549